UC Berkeley

UC Berkeley Previously Published Works

Title

A Balance between Inter- and Intra-Microgel Mechanics Governs Stem Cell Viability in Injectable Dynamic Granular Hydrogels.

Permalink

Journal

Authors

Morley, Cameron
Ding, Erika
Carvalho, Emily
et al.

Publication Date

DOI

A Balance Between Inter- and Intra- Microgel Mechanics Governs Stem Cell Viability in Injectable Dynamic Granular Hydrogels

Cameron D. Morley[1], **Erika A. Ding**[2], **Emily M. Carvalho**[2], **Sanjay Kumar**[1,2,3,4]

[1]Department of Bioengineering, University of California, Berkeley, CA 94720, USA

[2]Department of Chemical and Biomolecular Engineering, University of California, Berkeley, CA 94720, USA

[3]San Francisco Graduate, Program in Bioengineering, University of California, Berkeley-University of California, Berkeley, CA 94720, USA

[4]Department of Bioengineering and Therapeutic Sciences, University of California, San Francisco, CA 94158, USA

Abstract

Injectable hydrogels are increasingly explored for the delivery of cells to tissue. These materials exhibit both liquid-like properties, protecting cells from mechanical stress during injection, and solid-like properties, providing a stable 3D engraftment niche. Many strategies for modulating injectable hydrogels tune liquid- and solid-like material properties simultaneously, such that formulation changes designed to improve injectability can reduce stability at the delivery site. The ability to independently tune liquid- and solid-like properties would greatly facilitate formulation development. Here we demonstrate such a strategy in which cells are ensconced in the pores between microscopic granular hyaluronic acid (HA) hydrogels (microgels), where we tune elasticity with static covalent intra-microgel crosslinks and flowability with mechanosensitive adamantane-cyclodextrin (AC) inter-microgel crosslinks. Using the same AC-free microgels as a 3D printing support bath, we preserve the location of each cell as it exits the needle, allowing us to identify the mechanism driving mechanical trauma-induced cell death. We vary microgel AC concentration to find the threshold from microgel yielding- to AC interaction- dominated injectability and exploit this threshold to fabricate a microgel with better injection-protecting performance. Our delivery strategy, and the balance between intra- and inter-microgel properties it reveals, may facilitate the development of new cell injection formulations.

Graphical Abstract
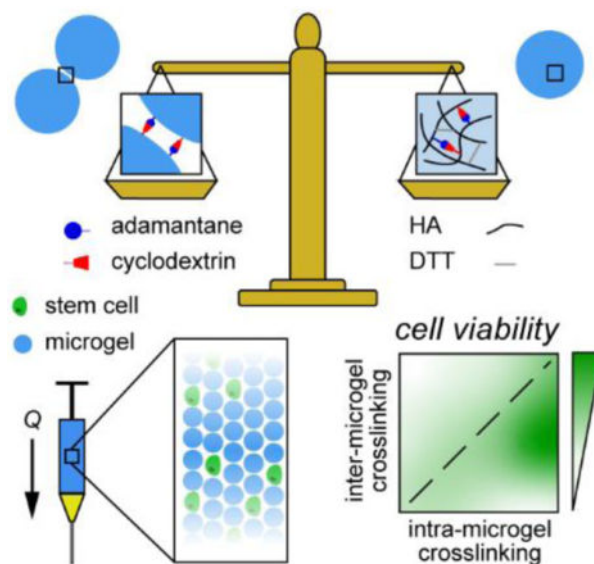
A guest-host injectable microgel formulation strategy is introduced in which flowability and elasticity are tuned independently by modulating inter- and intra-microgel crosslinking. Flowability and elasticity represent conflicting constraints in injectable design, with the former influencing injection protection and the latter regulating engraftment potential at the injection site. The balance between these parameters is systematically investigated and found to regulate stem cell viability during injection.

Keywords

microgels; injectable granular hydrogels; yield stress materials; 3D bioprinting; adamantane and cyclodextrin (AC)

1. Introduction

Administration of cell-based therapeutics has shown increasing promise for disease treatment and regenerative medicine. When the anatomical target is diffuse, such as in the case of bone marrow transplantation, cells may be delivered intravenously, leveraging diffusion and convection through the vasculature for distribution throughout the body. However, highly localized delivery of cells to solid tissues has proven much more challenging because the formulation must be sufficiently liquid-like to permit injection but sufficiently solid-like to remain at the target site. Encapsulation of cells in 3D hydrogels prior to injection into tissue is emerging as an attractive strategy to address the latter challenge[1–5]. Once delivered, hydrogels can provide a mechanically stable engraftment niche for engineered cells and thus improve cell survival and function[3,6]. However, the covalent crosslinking strategies often used to form these hydrogels can compromise injectability and potentially subject cells to mechanical trauma as the hydrogel can be damaged during injection[7,8]. Viability and engraftment in vivo can often fall below 5%[3,6], which has been attributed to the possibility that rheological characterization alone may inadequately capture the injectable's injection-protecting properties during flow through

thin needles and under the near-instantaneous deformation associated with hand injection[9]. Thus, there is a strong and open opportunity to improve the performance of shear thinning injectables by better defining relationships between injectable composition, flow properties, and cell viability.

Progress has been made by developing hydrogels with temporally tunable crosslinking kinetics, such as those employing click-chemistries[10–12] or self-healing materials that respond to external stimuli (e.g. pH or temperature)[13,14], and shear-thinning properties to facilitate flow during injection and control over solidification upon delivery[15–18]. An emerging mechanosensitive crosslinking approach creates dynamic noncovalent crosslinks using guest-host chemistries[19], such as adamantane and cyclodextrin (AC)[5,20], allowing for transient rupture and bond re-formation in response to shear stress. Hydrophobic and highly specific AC interactions[14,21] facilitate the rapid dissociation and re-association of bonds required to satisfy the two dominant goals of injectable cell carriers. While dynamic crosslinking strategies greatly improve protection of cellular cargo in cell therapies, they fail to fully address the trade-off between injectability and stability; enhancing performance in one property generally compromises the other. Independent tuning of material injection-protection and engraftment-facilitation is needed to improve the efficiency of cell therapies.

Packed microscale hydrogel particles (microgels), which are widely used in 3D cell culture and biofabrication[22–25], have recently been explored as a strategy for balancing injectability and injection-protection[26–30]. In the jammed state, these materials reconfigure and flow like liquids at high shear rates but also demonstrate solid-like yield stress properties at low shear rates[22]. The micro-porous architecture of microgels facilitates cell encapsulation between particles, which physically shields cells from intra-needle velocity gradients and high shear stresses at the no-slip boundaries. Previous studies have shown that particle shape and size influence injectability and engraftment[27,28], and dynamic inter-particle AC crosslinking improves injection-protection and viability for cells encapsulated between spherical but not irregularly shaped particles[28]. An appealing explanation for the latter result is that the increased contact area and inter-particle interaction associated with fragmented particles may alter rheological properties and consequently injectability and cell viability[28]. A deeper understanding of how the balance between intra- and inter-particle interactions affect cell injection and cell viability would facilitate customized injection-protection for future cell therapies.

In this study, we introduce an injectable formulation strategy in which spherical hyaluronic acid (HA) microgels are dynamically crosslinked with AC and decorated with RGD-based peptides to enable 3D integrin engagement. Just as the force-sensitivity of AC crosslinks has been exploited to fabricate stress-relaxing bulk hydrogels, we find that reversible AC crosslinks between microgel particles support the shear-thinning behavior needed for injectability while stabilizing the microgel pack post-injection with minimal residual stress. We demonstrate the ability to independently tune the elastic and flow properties of the microgel pack by varying HA and AC concentration respectively. We also explore the effects of the balance between static intra- and dynamic inter-microgel properties on injected cell viability.

2. Results

2.1. Microgels as an injectable and as a platform for injectable testing

2.1.1. HA microgel-based injection-protecting formulation—Guest-host microgel formulations have emerged as a promising strategy for cell delivery, primarily due to their injection-protecting nature. However, the governing principles that relate microscale mechanics within the microgel formulation to injection protection and injectability remain incompletely understood. We hypothesized that the flow properties of guest-host microgels are dictated by a balance between the intrinsic material properties of the microgels themselves and the strength of the AC bonds between microgels. We further reasoned that we could tune cell survival by first modifying inter-microgel interactions alone.

To systematically explore these governing principles, we fabricated spherical HA microgel assemblies stabilized by two types of crosslinks: static covalent linkages to set intrinsic microgel mechanical properties, and dynamic AC-based inter-microgel crosslinks that can break and reform. To introduce chemical handles for both crosslinking and peptide conjugation, we methacrylate-functionalized HA (MeHA) (Methods, Figure S1)[31,32]. We then fabricated monodisperse (n = 100 measurements, PDI = 0.01), 10.0 μm diameter (Figure S2a–c) spherical microgels by reacting 2% (w/w) MeHA with a 1,4-Dithiothreitol (DTT) crosslinker in the aqueous phase of an inverse emulsion (Methods, Figure 1a). We tuned the microgel diameters to be cell-sized, minimizing intra-needle velocity gradients by ensuring that both cells and microgels are roughly 10× smaller than the 200 μm (27 – 30G) cannula diameter commonly used in delivery of cell therapies[9] (Figure 1b). We functionalized the microgels with RGD and AC, centrifuged them to mimic the mechanical properties of their bulk hydrogel counterparts (Methods, Supplementary Information, Figure S3b), and mixed them with cells before testing their efficacy at reducing intra-needle shear stress and facilitating 3D engraftment (Figure 1c).

2.1.2. Material platform validation – neural stem cell (NSC)-microgel attachment—Prior to mechanically characterizing the governing relationships between microgel mechanics, injectability, and cell viability, we sought to establish the baseline ability of our microgel formulation to support cell adhesion and function, particularly the ability to form multicellular assemblies, protrusions, and cell-cell connections. For our studies, we chose to work with murine neural stem cells (NSCs, Methods), which can give rise to neurons in the brain and show great promise as injectable cell sources in neuroregenerative applications[3,33,34] but suffer from low rates of engraftment. To facilitate NSC attachment, we functionalized the microgels with an RGD-based adhesive peptide (Methods) and gently pipette-mixed them with NSCs to create homogenous 3D cellular dispersals.

NSC viability was sensitive to 2D seeding density, leading us to consider the effect of seeding density on viability and attachment in 3D as well. We found seeding densities, ϕ_0, below 10% (v/v) to have low viability in bare microgels beyond 3 days in culture (Figure S4), so we examined attachment of NSCs seeded at $\phi_0 = 10\%$ in microgels functionalized with 0 – 0.2 mg mL^{-1} RGD peptide. After 24 h in 3D culture, NSCs

in microgels of all RGD concentrations microgels self-assembled into spheroids and began extending protrusions into the microgel pack (Figure 2a, S6). With additional time in culture, protrusions began to connect spheroids, where we noticed the z-position of spheroid-connecting protrusions depended on RGD concentration. NSCs cultured in bare and 0.002 mg mL^{-1} RGD microgels generated protrusions only at the interface of the glass bottom of the well (z = 0 μm) (bottom panel, Figure 2a,b, Methods), indicating that NSCs do not efficiently form 3D connections in these conditions. Instead, only small, discrete spheroids are observed at large z-depths (white circles, Figure 2a, bottom). In contrast, network-forming protrusions can be observed hundreds of microns above the glass bottom in 0.02 and 0.2 mg mL^{-1} RGD microgel packs (Figure 2a,b). Increasing NSC density to 20% (v/v) led NSCs to assemble more quickly (Figure 2b) but with shorter connecting protrusions. The slower NSC assembly with greater cell-to-cell distance (Figure 2b) is consistent with previous studies demonstrating a percolation threshold for cellular dispersals in granular media[25]. Based on these results, we used 10% (v/v) cell densities in subsequent injection experiments.

2.1.3. Material platform validation – NSC injection into hydrogels—Based on the expectation that cells could attach to the injected matrix in 3D, we next asked whether the microgel injectable improves NSC engraftment potential by retaining more injected cells. We injected NSCs mixed with either liquid medium or bare HA microgels into bulk HA hydrogels using the injector of our 3D bioprinter (Figure 3a, Methods). While this injection strategy is a heavily abstracted model of in vivo injection, the use of a hydrogel target rather than tissue enabled us to visualize the injected volume to measure the retained injectable volume, V_r, with confocal microscopy. Moreover, the use of precise linear motion stages allows us to delicately enter tissue-like hydrogels and evaluate the volume of cargo retained when injected into viscoelastic solids. After 12 h of 3D culture post-injection, we observed viable cells in both the microgel and liquid media injectables, albeit with distinctly unique injected volumetric morphologies (Figure 3b). In contrast, the yield stress capability of the microgel injectables reinforced the cracks generated by injection and deformed the hydrogel to create a larger oval-shaped cavity (Figure 3b). We measured a 7.5-fold increase in retention volume for the microgel injectable relative to the liquid medium control (p<0.01) (Figure 3c, Methods and Supplementary Information).

2.1.4. 3D printing into microgels: determining sources of mechanical trauma in granular injectables—Having established that our microgel formulation supports NSC adhesion, viability, and retention upon injection into hydrogels, we next investigated the ability of our microgel-based formulations to support injection protection and cell viability during injection using our 3D bioprinter (Figure 1c). We compared the performance of our microgel formulations against control conditions in which NSCs were suspended in non-crosslinked hydrogel precursor solutions. Testing injectable efficiency using this embedded 3D printing approach holds many key strategic advantages. Precise control of flow rate with our 3D printer enables prediction of intra-injectable stresses when coupled with rheological characterization. Most importantly, embedded printing in microgels (Figure 1c – *I*, Supplementary Information) preserves the spatial distribution of cells as they exit the needle, allowing us to identify localization of cell damage. When injecting Newtonian

or shear thinning liquids, for example, we would expect mechanical stress-induced cell death to be highest at the needle wall and gradually decrease toward the center of the needle. If this cargo was being injected into liquid media, the shear history of each cell would be lost, eliminating the ability to directly observe cell death at the no-slip, high shear stress boundary. Access to injection history could be informative in developing injectable formulations, especially for non-Newtonian or granular microgel injectables, where the flow profile is rate-dependent and underlying injection-protection limitations are still poorly understood[9,28].

To first demonstrate that embedded 3D printing preserves the injection history and quantify the shear stress required to damage NSCs, we printed mixtures of NSCs with the microgels' Newtonian liquid precursor, 3% (w/w) uncrosslinked MeHA, into bare (i.e. free of AC and RGD) HA microgels. We chose the MeHA concentration by identifying the viscosity and shear rate required to generate 5 – 100 Pa of shear stress at the needle wall, as previous reports document cell death and membrane rupture between 30 – 150 Pa[35,36] (Figure 4a, Supplementary Information). To increase shear stress, we varied shear rate from 250 – 4125 s^{-1}, and modified printing needle translational velocity proportionally to achieve 300 μm printed diameters, thereby minimizing potential negative effects of nutrient depletion at the center of printed NSC features in 3D culture. We confirmed the Newtonian fluid-like behavior of MeHA by showing $\sigma \sim \dot{\gamma}$ across the range of tested shear rates with unidirectional rheology (Figure S3a). We predict printed feature cross-sectional area, A, similar to our previous reports[22] (Methods, Figure S7). In these MeHA prints, we observed increased cell death (red, Figure 4a, Methods) with increasing shear rate and localization of dead cells at the outermost layer of the printed object.

We repeated the shear rate sweep with mixtures of bare microgels and NSCs into bare HA microgels and found increased cell viability relative to their liquid MeHA counterparts. However, cell viability at the highest shear rate still fell below 70%, which is required for FDA approval of injectable cell formulations[37]. In contrast to the MeHA prints, we observed dead cells and increasing co-localization of the live and dead channels distributed throughout the printed feature, suggesting shear stress is instead generated between microgels. We hypothesized that cellular damage could be driven by increased frequency of microgel rearrangement and speed at which microgels slide past one another at high shear rates.

To suppress microgel rearrangements and consequent intra-injectable shear stress, we printed mixtures of NSCs and AC-functionalized HA microgels into bare HA microgels. We functionalized our HA microgels with AC concentrations of 0.01 (low), 0.05 (medium), and 0.11 (high) molecule-to-HA monomer repeat unit molar ratio and repeated the injection shear rate sweep (Methods). We found that the low and medium AC densities support higher cell viability than MeHA, bare HA microgels, and high-AC microgels (Figure 4b). We then sought to further evaluate the performance of the AC microgel injectables under more realistic injection speeds, so we performed injections by hand (Methods) which we predict generates a shear rate 5-fold higher than the maximum shear rate of our 3D printer. Strikingly, we found that viability fell with increasing AC concentration ($p<0.01$), and low AC concentration yielded 70% NSC viability (Figure 4b).

2.2. Determining the mechanism for decreased cell viability in high AC concentration microgels

The reduced cell viability in the high-AC concentration microgels suggests that increased microgel-microgel adhesion alters rheological properties in a way that reduces injection protection. Control experiments revealed that the cytotoxicity seen in these formulations could not solely be attributed to physical NSC-microgel contact or unreacted AC reagents (Methods, Supplementary Information, Figure S4, S5a, S8). We also began to observe shear rate dependent increases in cell death as early as 24 h post-injection (Figure S9). These studies support the notion that mechanical trauma dominantly contributes to cell death in our system. We also therefore chose to evaluate cell viability at 24 h post-injection in subsequent experiments.

Cell viability in our microgel injectable formulations appears to be independent of radial position, in contrast to injection with MeHA solution, implying that the microgels protect the NSCs from injection trauma at low shear rates. As shear rate increases, cell death increases throughout the microgel but remains radially independent, implying that higher shear rates induce trauma driven by microgel rearrangement. The factors governing inter-microgel mechanics are the microgel yield stress, which is a function of intrinsic microgel material properties, and AC bond density. To quantify these factors, we probed microgel pack mechanics using rheology and HA hydrogel surface mechanics using atomic force microscopy (AFM).

2.2.1. Rheological characterization of AC microgel packs

We first performed oscillatory rheology to measure the elastic storage modulus, G', and the loss modulus, G'', of each AC microgel condition (Figure 5a). For all AC concentrations, G' was frequency-independent and greater than G'', indicating dominantly solid-like behavior at low strain. Further, we observed minimal changes in low-strain mechanical properties with increasing AC concentration, which is expected due to the molar ratio of DTT being much larger than that of the AC (Methods). Despite observing changes in G' that vary by less than a factor of two across all samples, we observed up to a 5-fold increase in G'' between the high AC concentration and bare microgels. This demonstrates that intra-microgel AC dominantly contributes to G'' in the limit of a much higher molar ratio of DTT, enabling us to tune elastic and flow properties independently. We then performed unidirectional rheology on the AC microgels and found that bare and low AC microgels behave as Herschel-Bulkley (HB) yield stress fluids (Methods, Figure S10a). At low shear rates, $\dot{\gamma}$, HB materials display a plateau in shear stress, denoted as the material yield stress, σ_y, and at high shear rates they showcase constant, sub-Newtonian flow, where $\sigma \sim \dot{\gamma}^{<1}$. In contrast, medium and high AC concentration microgels do not have the characteristic plateau at low shear rates and can often display slip-like events, indicated by gradual increase followed by a rapid decrease in σ (Figure S10b). Shear stresses at a given single shear rate can also vary by more than half an order of magnitude (Figure 5b).

We repeated the oscillatory and unidirectional characterization of bare HA microgels from different MeHA stocks and microgel fabrications to ensure reproducibility of the aberrant rheological properties (Figure S10a,c). The measured G' and σ_y vary by less than a factor

of 2, which is much less than the 5-fold change observed in σ_y for medium and high AC concentrations (Figure 5b). Thus, we attributed the small variation in bare HA microgel rheological properties to errors in sample preparation. Past studies have demonstrated that microgels display the linear scaling relationship, $G' \sim \sigma_y$[22,25,38]. This relationship was leveraged to both account for sample preparation variability, as changes in G' would be reflected in σ_y, and to isolate the effect of AC bonds on flowability. For a given sample, we normalized σ from unidirectional rheology by its respective average G' from oscillatory rheology (Figure 5a) resulting in the expression, $\sigma/\langle G'(\omega)\rangle_\omega$, where ω is frequency, and plotted the average calculated values (n=3 samples, Figure 5b) with error bars corresponding to the minimum and maximum shear stress at each shear rate.

These normalized data confirm the classification of the bare and low AC microgels as HB materials, where forced flow in these microgel packs generates measured σ_y on the order of 10% of G' and with minimal variation in σ for all shear rates. In fitting the bare and low AC microgels to the HB model, we found that the magnitude of the power-law increase in σ at high $\dot{\gamma}$ decreased with increasing AC concentration (Table 1). The trend of decreasing power-law with increasing AC concentration continues with the medium and high AC samples, suggesting that flow becomes less Newtonian and more shear thinning. However, the aberrant unidirectional rheology flow profiles for medium and high AC concentrations suggest that inter-microgel AC bonds are playing a larger role than the microgel yield stress during injection. We expect the maximum shear stress during microgel rearrangement to correspond to the bare microgel yield stress; however, AC bonds connecting microgels must break prior to microgel yielding for this to be true. We therefore sought to quantify the maximum shear stress arising from microgel rearrangement, and experienced by cellular cargo, by applying an instantaneous step-shear to our HA-AC microgel formulations and measuring their relaxation moduli, G'_r (Figure 5c,d). We quantified the peak relaxation modulus, $G'_r(0)$, normalized by the samples' respective average G' from oscillatory rheology and observed an increasing maximum shear stress with increasing AC concentration (Figure 5c). The peak relaxation moduli of the bare and low AC concentration microgels were statistically indistinguishable, and their magnitude closely matches the bare microgel yield stress, corroborating our expected result. In contrast, instantaneously applied shear on high AC microgels can result in shear stresses up to five times the bare microgel yield stress. The values of peak relaxation moduli in medium and high AC microgels far exceed the bare microgel yield stress, suggesting yielding and microgel rearrangement are set by the strength of inter-microgel AC bonds instead of the microgel yield stress. The discrepancy between these peak moduli values and shear stress at low shear rates in unidirectional rheology support the idea of highly unpredictable and rate-dependent flow properties for medium and high AC concentration microgels.

Examination of G'_r over time, t, reveals a power-law relationship (Figure 5d). Fitting these curves to the equation, $G'_r(t) = t^{-\beta}$, where β is the slope of the relaxation curve on a log-log scale, reveals increases in the magnitude of β with increasing AC concentration (Table 1). While the mechanism behind this scaling law requires further study, we attribute this feature

to an increased rate of AC bond re-formation, likely due to increased AC bond density, after large shear events.

Taken collectively, we hypothesize that low AC concentrations enable the microgels to ease rearrangement during flow, protecting cellular cargo better than their bare microgel counterparts. This hypothesis is supported by the observation of a lower power scaling between σ and $\dot{\gamma}$ (Table 1). However, when AC bond density increases above a certain threshold, we reasoned that the stress required to break bonds at the microgel-microgel interface could be greater than the microgel yield stress, increasing the frequency and magnitude of microgel yielding and damaging cellular cargo.

2.2.2.   Quantifying the stress to break AC bonds—To quantify AC bond stress, we performed atomic force microscopy (AFM) on bulk HA-AC hydrogels with an adamantane-functionalized probe (Methods, Figure 6a). We observed a non-linear relationship between force and indentation depth, as measured by displacement into the sample (Methods), d, on the approach curve (red, Figure 6b) between the adamantane-functionalized probe and all HA-AC hydrogels. The retraction curves (blue, Figure 6b) revealed large adhesion events; we observed a negative measured force when $d = 0\ \mu m$ and negative measured values of d when the probe disengages with the hydrogel (black circle, Figure 6b). We analyzed the approach curves to calculate the elastic modulus, E (Figure 6b,c), and retraction curves to measure adhesivity, extracting work of adhesion, W_a, and maximum adhesion force, F_a (Methods, Figure 6b). To ensure that the adhesion events were AC-specific, we performed indentations on HA-AC hydrogels with a bare probe. We observed that W_a and F_a fell in the measurement noise floor, closely mimicking the bare probe on bare hydrogel indentations (Figure S11a). Fitting the data on the approach curves of these indentations, we calculate elastic moduli just above 1 kPa (Figure 6d). Using measured values of Poisson's Ratio for these hydrogels (Figure S12) and using the equation, $E = 2G'(1 + v)$, we find agreement between our rheological and AFM characterization (Figure 6d). This finding further corroborates the finding that AC contributes minimally to elasticity in this formulation.

In characterizing the retraction curves of HA-AC hydrogels indented with the adamantane-functionalized probe, we found adhesion increased with increasing AC concentration (Figure S11b,c) and was minimal when indenting a bare hydrogel. This trend led us to conclude that adhesion is dominated by specific AC interactions. We observed large adhesive forces over large retraction distances prior to AC bonds disengagement, leading us to calculate W_a. We found that W_a increased with increasing AC concentration (Figure 6e). We calculated adhesive stress during AC bond-breaking by dividing F_a by the maximum measured probe contact area, A_p (Methods). We also observed increasing adhesive stress with increasing AC concentration (Figure 6f) and sought to compare these values to the bare microgel yield stress. Since only half of the AC molecules are engaged during these experiments, we assume that we only measure half the stress required to break AC bonds between adjacent microgels. Thus, to compare the magnitude of the yield stress to the magnitude of the stress generated during AC bond-breaking between microgels, we compared the adhesive stress (Figure 6f) to half the bare microgel yield stress. Strikingly, we find the adhesive stress of

the low and medium AC concentrations straddle the microgel yield stress line, supporting the hypothesis that breaking bonds in medium and high AC concentration microgels require stresses larger than the bare microgel yield stress. This conservative approximation further supports the idea that a balance between two forces dictates injectability and cell survival in granular guest-host microgels.

2.2.3.   Exploiting the AC bond strength and microgel yield stress threshold

—The AFM results suggest that either decreasing the AC concentration or increasing the microgel yield stress could improve injected cell viability. The former would decrease the stress required to break inter-microgel connections, and the latter would increase the stress that the microgel pack could withstand upon AC bond breaking events. To test this hypothesis and determine if the low AC concentration microgels were optimal for the 2% (w/w) microgel formulation, we fabricated microgels with 0.001 and 0.005 AC:HA ratios. We repeated hand injections with these microgels and compared their injection-protecting performance against bare microgels (Figure S13a). However, we observed that lower AC concentrations resulted in marginally reduced viability that neared bare microgel injection levels (Figure S13c) and AC-specific adhesivity similar to that of bare hydrogels (Figure S13b).

We then tested the hypothesis that increased microgel yield stress could improve cell viability. To make microgels with a higher yield stress, we increased the MeHA concentration to 4% (w/w), fixing the DTT-to-HA monomer ratio at 0.7 and varying the AC molar concentration from 0.32 – 3.15 mM (Table 2). Oscillatory rheology shows that bare 4% (w/w) microgels have G' of 3000 Pa and σ_y of 80 Pa, roughly 7.5- and 4-fold increases in these properties with respect to the 2% (w/w) microgels (Figure S14). The yield stress of the 4% (w/w) microgels is twice the magnitude of the highest measured adhesive stress in the 2% (w/w) and 3.15 mM AC microgels, so we anticipate injection with this formulation would yield higher cell viability. We repeated the hand injection experiment (Figure 7a) and found viability substantially increased with the 4% (w/w) AC microgels relative to their 2% (w/w) counterparts for all AC concentrations. From this result, we conclude that granular guest-host injectable performance relies heavily on the interplay between microgel yield stress and collective AC bond strength.

3.   Discussion

In this study, we examined rheological factors governing cell viability in granular guest-host injectables. Spherical bare microgels behaved as HB yield stress fluids and protected cellular cargo from mechanical trauma at low shear rates. We attribute injection protection of bare microgels to generation of plug-like flow; shear stress magnitudes measured with unidirectional rheology approached values we anticipate would damage cellular cargo at shear rates as low as 100 s^{-1} (Figure S10), a factor of 10 lower than the injected shear rate of 1250 s^{-1} where we found NSC viability to be 70%. This suggests that injection protection extends well into the sub-Newtonian flow regime. Viability decreased with increased shear rate but was not dependent on radial needle position, suggesting mechanical trauma arose from inter-microgel rearrangements (Figure 4) which must occur during injection. For example, microgels and NSCs rearrange as they flow from large diameter syringes or luer-

lock adapters to thin needles. During rearrangement, microgels yield and NSCs experience stress magnitudes that correspond to the yield stress (Figure 5). Interestingly, the 20 Pa yield stress for 2% (w/w) microgels falls near the stress magnitudes observed to damage cells[35,36]. For 4% (w/w) and 80 Pa yield stress microgels, we observed a decrease in viability ($p<0.05$) relative to the 2% (w/w) microgels (Figure 7b S14c), further implying that the stress magnitude cells experience during microgel yielding can damage cellular cargo. These findings collectively suggest an interplay between yielding rate and microgel elasticity dictating cell viability in AC-free systems. Future studies that enable visualization of microgel architecture during high shear rate injection could provide direct support for these ideas.

We observed a small increase in viability between 2% (w/w) bare and low AC concentration microgels followed by rapid decrease in viability for medium and high concentration AC microgels (Figure 4, S13). We attribute low viability with medium and high AC concentration microgels to an inability of the microgel yield stress to support microgel dislocation associated with AC bond rupture (Figure 5). We reasoned that AC-driven microgel yielding is not supported by the bulk microgel yield stress; rupture of inter-microgel AC bonds dislocates microgels at high shear rates, damaging cellular cargo. An effective injection protecting microgel should have microgel yield stresses that exceed the stress of inter-microgel AC bond breaking, enabling new AC bonds to form and for microgels to gently roll past one another. Thus, to suppress the negative effects associated with AC-driven yielding, stiffer microgels with higher yield stresses are required. In characterizing AC bond strength, we anticipated a linear relationship between AC molecule to HA-monomer repeat unit and work of adhesion, and for additional AC bonds to behave as an increased number of elastic spring elements per unit area. However, we found that 5- and 10- fold increases in the AC molecule to HA-monomer repeat unit ratio between the low-medium and low-high AC concentrations respectively resulted in 2- and 6- fold increases in the calculated work of adhesion and 2- and 4-fold increases in adhesive stress. While this relationship should be explored further in future studies, the seemingly non-linear relationship between AC concentration and adhesion suggests that HA elasticity within the microgel could be coupled to AC bond strength. This finding indicates that internal microgel stiffness can also play a large role in granular injectable systems utilizing AC interactions and suggests that microgels can deform and store energy as AC bonds are strained. This crucial finding has implications for understanding the effect of AC bonds on other granular injectables, where cell viability has shown to be dependent on microgel geometry[28]. Increased engagement of AC bonds, whether through higher contact area due to changes in microgel size and geometry or AC density, leads to a non-linear elastic response whose mechanics depend heavily on yielding and intra-microgel properties.

4. Conclusion

Using a microgel platform in which we can independently control elasticity and flowability, we elucidated a mechanistic force balance between inter- and intra-microgel mechanical properties that governs stem cell viability during injection. The best-performing granular injectables had yield stresses that were greater than the stresses required to break AC bonds. Key to this discovery was our use of oscillatory rheology to probe intra-microgel

mechanics and unidirectional rheology and AFM to quantify flowability and strength of AC adhesion. Our study was also facilitated by a 3D printing-based method to screen our injection-protecting injectables, where the ability to control and observe the spatial distribution of cells during injection enabled us to explore the effect of the interplay between inter-particle adhesion and microgel yield stress on injection protection and cell viability. We anticipate this platform to have utility in tuning injection-protection and intra-tissue retention independently for an array of cell types, polymer backbones, and target tissues. This tuning capability could advance existing regenerative medicine approaches, such as cell replacement for myocardial infarction (MI) and type-I diabetes[28,39–41], leveraging granular injectables.

5. Methods

5.1. Cell culture

Murine neural stem cells (NSCs) isolated from the cortices of embryonic day 15 – 18 C57/BL6 mice were obtained from Sigma Aldrich (SCR029). NSCs were cultured according to supplier protocols. Briefly, tissue culture dishes were coated with 20 μg mL^{-1} poly-ornithine and 10 μg mL^{-1} laminin stepwise overnight. Mouse NSC expansion media (Sigma Aldrich, SCM008) was used to culture NSCs on the coated tissue culture dishes and to swell the microgels. NSCs were cultured at 37 °C and 5% CO_2 in 2D where half-media changes were performed every other day until reaching 80 – 90% confluency. To ensure effects of nutrient depletion are minimized during 3D microgel culture, experiments extending beyond 24 h were supported by 50% daily media exchanges. Cells were confirmed to be negative for mycoplasma; testing occured every 3 – 4 months with the Agilent MycoSensor QPCR Assay Kit.

5.2. Methacrylation of Hyaluronic Acid (HA)

Methacrylated hyaluronic acid (MeHA) was prepared as described previously[31,32]. Briefly, HA (Lifecore Biomedical, HA60K-5) with a nominal molecular weight of 60 kDa was suspended in deionized water at a maximum of 1 % (w/w). The solution was continually stirred, placed on ice for the remainder of the reaction, and 8 mL of methacrylic anhydride (Sigma Aldrich, 760-93-0) per gram of HA was added dropwise (approximately 10-fold excess relative to the disaccharide repeat unit). The pH was maintained between 8 – 9 using NaOH for 6 – 8 h. The reaction is continued overnight at 4°C to achieve 98% functionalization (Figure S1). To collect the MeHA, chilled ethanol was added in ten-fold excess to the solution causing the MeHA to precipitate out. The mixture was centrifuged, ethanol was aspirated, and the MeHA was resuspended in deionized water. The resuspended MeHA was vacuum filtered through a 0.22 μm filter to remove unreacted methacrylate anhydride. The solution was stored at −80°C overnight and lyophilized for long-term storage. ^{1}H-NMR spectra were collected on a Bruker Avance AVB-400 at 400 MHz. Methacrylation efficiency was calculated as the ratio of vinylic protons on the methacrylate group to the N-acetyl methyl protons on the HA backbone, normalized to the number of protons per group (Figure S1).

5.3. Microgel fabrication and functionalization

To fabricate HA microgels, we crosslinked hydrogel droplets in an inverse emulsion. The aqueous phase consists of 2% (w/w) MeHA and crosslinker 1,4-Dithiothreitol (DTT) with a 0.7 thiol:HA monomer repeat ratio, and the organic phase consists of kerosene and 1.25% (w/w) Span-80 (Sigma Aldrich, S6760-250ML). The concentrations of each component in the aqueous phase were determined by fabricating bulk hydrogels and performing oscillatory rheology, where we chose parameters that generated hydrogels with 400 Pa storage moduli to mimic the mechanical properties of the brain parenchyma (Figure S3b). The resulting solution was homogenized using the Bio-Gen PRO200 (Pro Scientific, 01–01200) to create smaller and monodisperse emulsion droplets. The Michael Addition reaction was performed by mixing on ice for a minimum of 4 h. Once crosslinked, the organic phase was removed from the mixture. To remove excess kerosene and surfactant, the microgels were serially washed with 0.1% (v/v) Tween 20 in PBS (Sigma Aldrich, P1379–25ML). Wash steps are performed by diluting the microgel pellet by a minimum of a factor of 1000 (v/v) for each wash.

Inter-microgel adhesion was tuned using a custom adamantane peptide (Adamantane-KKKCG) and cyclodextrin (Tocopharm, 81644-55-5). From the rheological data (Figure S3b), we show that centrifugation of HA microgels at $4000 \times g$ yields G' values that approach the bulk hydrogel limit. Previous studies have shown that small-strain oscillatory rheology probes intra-microgel mechanics; therefore, the MeHA concentration within each microgel is near their bulk hydrogel counterpart (2 % w/w). The monodispersity and spherical geometry of our microgels (Figure S2) enables us to assume that they are randomly close-packed and have a solid volume fraction of 64%. Thus, we calculate the average MeHA molarity to be 28.6 mM by multiplying the intra-microgel MeHA concentration by the approximate microgel solid volume fraction and dividing by the molecular weight of MeHA (MW = 447.39 g/mol). We then calculate the required molarity of adamantane (MW = 725.0 g/mol) and cyclodextrin (MW = 1151.05 g/mol) to achieve the desired molar ratios (Table 2).

We centrifuge bare microgels at 4000 $\times g$ for 5 min, aspirate the PBS supernatant, gently pipette mix the pack without introducing air bubbles with a positive displacement pipette, remove 500 μL of the packed microgels, and place the microgel suspension a 1.5 mL Eppendorf tube. Adamantane stock solution is added first and left for a minimum of 2 h on a shaker. To remove unreacted molecules, we resuspend the microgels an additional 1 mL of PBS, centrifuge at 15,000 $\times g$ for 30 s, and aspirate the PBS, repeating this process six times to achieve a 1000-fold dilution of unreacted molecules. Microgels are centrifuged at 4000 $\times g$ for 5 min after rinsing and the supernatant is aspirated. We repeat the functionalization and rinse protocol with cyclodextrin. The microgel pellet is resuspended in 14.5 mL of NSC growth media and moved into a 15 mL centrifuge tube. The mixture is left at 4°C overnight, centrifuged at 4000 $\times g$ for 5 min, the supernatant is aspirated, and the microgels are resuspended in 14.5 mL of NSC media to achieve a 1000-fold PBS dilution before use.

Reported concentrations of 0.01 (low), 0.05 (med), and 0.11 (high) correspond to the individual guest or host molecule to HA monomer repeat unit ratio. Thus, we approximate that 2, 10, and 22% of the HA repeat units bear AC molecules. These concentrations were

chosen as the methacrylation protocol used here yields 98% efficiency (Figure S1) and 70% of the HA repeat units are used for DTT crosslinking. The remaining 28% of available methacrylate groups for AC provided a sufficient dynamic range of rheological properties for this HA-DTT concentration. The same procedure was used to functionalize microgels with integrin binding peptide (Anaspec, AS-62349).

5.4 Ellman's reaction

To determine the efficiency of our protocol for AC functionalization of HA microgels, we performed an Ellman's reaction. We separately prepared 20 μL of microgels with 3.15 mM adamantane, 3.15 mM cyclodextrin, and 3.15 mM AC added sequentially as described previously. We chose the high AC concentration microgels for this experiment to provide the most conservative approximation of the reaction efficiency due to this formulation having the lowest predicted post-functionalization methacrylate group availability. We resuspended the 20 μL microgel pack with 20 μL of fresh PBS, centrifuged the mixture at 4000 $\times g$ for 5 min, and collected the supernatant. We prepared a reaction buffer (100 mM sodium phosphate, pH 8.0, 1 mM EDTA) following the manufacturer's instructions for 5,5-dithio-bis-(2-nitrobenzoic acid) (Ellman's Reagent, product no. 22582). We added 200 μL of reaction buffer and 4 μL of 4 mg mL^{-1} Ellman's Reagent to each supernatant and measured the solution's absorbance at 412 nm. Data were normalized to a standard curve of each solution. We found that the unreacted adamantane and cyclodextrin in the supernatant fell below the detection threshold of 0.1 mM, thus yielding a greater than 96% reaction efficiency (Figure S8b). When AC was added sequentially, we found 10% of the cyclodextrin added to be unreacted. We also performed this reaction on the supernatant of the sequential AC reaction after performing our rinse protocol (Methods) and found that all the unreacted cyclodextrin molecules had been removed from the solution. The Ellman's reaction could not be repeated for unreacted RGD because the highest RGD concentration of 0.2 mg mL^{-1} (0.19 mM) used in the manuscript fell near the detection threshold.

5.5. Rheology on HA microgels and MeHA

To characterize the mechanical properties of the microgel packs, we performed oscillatory, unidirectional, and step-strain rheology on an Anton Paar 302 rheometer with a 25 mm plate-plate configuration and a 1 mm gap. We centrifuged microgel samples at 4000 $\times g$, removed the liquid supernatant, and pipette-mixed before loading onto the rheometer. Oscillatory rheology used throughout all studies applied a 1% strain across frequencies ranging between 10^{-2} and 10^2 Hz. Unidirectional rheology was performed between shear rates of 10^{-2} and 10^3 s^{-1} and the results are fit to the Herschel-Bulkley (HB) model, $\sigma = \sigma_y \left(1 + \left(\frac{\dot{\gamma}}{\dot{\gamma}_c}\right)^p\right)$, where σ is the measured stress, σ_y is the yield stress, $\dot{\gamma}$ is the applied shear rate, $\dot{\gamma}_c$ is the critical shear rate at which the stress response changes from solid- to fluid-like and p is related to flowability at high shear rates. To determine the stress relaxation capabilities of the AC microgels, we applied a 50% step-strain and measured the stress response and fit the curves to the power-law model, $G'_r(t) = t^{-\beta}$. Unidirectional rheology was also used to determine 15 – 60 mg mL^{-1} MeHA viscosity, varying the shear rate between 10^{-2} and 10^2 s^{-1} (Figure S3a).

5.6. AFM on HA hydrogels

HA hydrogels were prepared by pipette mixing 2% (w/w) MeHA and 0.7 molar ratio DTT. 20 μL droplets were placed on polystyrene tissue culture dishes and immediately submerged in kerosene with 1.25% (w/w) Span80 to mimic the inverse-emulsion microgel synthesis. Samples were crosslinked for a minimum of 4 h. The organic phase was removed from the tissue culture dish and the samples were washed with PBS or PBS and 0.1% (v/v) Tween 20. The hydrogel droplet was left to swell in PBS overnight. Similarly, AC was added stepwise overnight. The AC solutions were removed before performing AFM.

Force measurements were performed on a MFP3D-BIO (Oxford Instruments) AFM using gold-coated pyrex-nitride probes (NanoWorld, PNP-Tr-AU) with nominal spring constant 0.08 N/m. Each probe was calibrated before use by the thermal method. A force trigger threshold of 1– 5 nN was used, and indentation depth was limited to 2 μm. We calculated indentation depth, d, by subtracting probe deflection from the piezoelectric motor position. All measurements were performed in PBS at room temperature. The contact and detachment point were identified for each indentation curve and are denoted by the origin and open black circle respectively (Figure 6b). The approach curve (red) is used to calculate elastic modulus, E, and the retraction curve (blue) is used to calculate adhesive work, W_a, and maximum adhesion force, F_a (Figure 6b). To calculate E, we fit the approach curve to the conical indentation variant of the Hertzian contact model given by the equation,

$$F = \frac{2E\tan(\alpha)d^2}{\pi(1 - v^2)},$$ where F is the force bending the cantilever, α is the probe half-angle, and

v is Poisson's ratio, which is measured separately to be 0.45 and is comparable to previous reports[42,43] (Figure S12). Using the measured Poisson Ratio and manufacturer reported probe geometry, we found that the conical Hertzian contact model with a single fitting parameter, E, generated curves falling directly on top of our measurements (Figure 6c). During fitting, E is constrained to 0.1 – 5 kPa. To calculate adhesive stress, we determined the peak adhesive force upon probe retraction, F_a. This value was divided by the maximum contact area, A_p, which we calculated based on the maximum identified probe penetration depth.

Probes were adamantane-functionalized based on published protocols[44]. In brief, gold-thiol reactions were performed by gently submerging the gold-coated probe in 1 mM adamantane solution overnight, then thoroughly rinsing with deionized water before use. We assume a higher adamantane density on the functionalized gold probes than on the AC functionalized hydrogels, making hydrogel-bound cyclodextrin, rather than probe bound adamantane, the limiting factor in adhesion measurements.

5.7. 3D printing preparations and hand injections

To facilitate fluorescence imaging and assaying of various shear rates within one sample preparation process, we pipetted 75 μL of microgels prepared at $1{\times}g$ and up to 75 μL of liquid media are pipetted into in glass bottom 96-well plates. To ensure the microgels settled to the bottom of the well, they were gently agitated and incubated at 37 °C for 10 minutes. When the NSCs reached 80 – 90% confluence in 2D, we removed the cells from the tissue

culture dish by incubating with Accutase for 5 minutes. The cells in solution were placed in a 15 mL centrifuge tube and centrifuged at 200 $\times g$ for 5 minutes. The Accutase was aspirated, and the cell pellet was diluted to achieve the desired cell density. NSCs were gently pipette-mixed into MeHA or HA microgels that were centrifuged at 4000 $\times g$ for 5 min. The resulting solution of MeHA or HA microgels with NSCs was loaded into the back of a 100 μL Hamilton gas-tight syringe. The plunger was slowly pushed through the syringe until the solution reached a 30G luer-lock affixed to the syringe. Before injection through the needle, we loaded the syringe onto the 3D printer, where the pump velocity was set to the lowest experimental flow rate. We jogged the pump until a small sphere of cells and matrix form at the needle tip. To perform hand injections, we manually displaced 5 μL in approximately 1 s, where we would predict the shear rate to be 20,000 s^{-1}.

5.8. Cell viability measurements and calculations

Cell viability was determined using the Live/Dead assay (Thermo Fisher, L3224) following manufacturer protocols. Live/dead images were acquired using a Zeiss LSM 710 confocal and images used in calculating feature size measurements were acquired using a Nikon TE2000-E epifluorescence microscope. We calculated cell viability manually isolating the central plane of the printed feature within a 3D confocal z-stack. For experiments where NSCs aggregated and single cells could not be identified to calculate viability using manufacturer protocols (Supplementary Information), we approximated live and dead cells to occupy the same area within a given plane and performed viability calculations with the equation $\% viability = 100\% \times \frac{live\,cell\,area}{total\,cell\,area}$. To determine total cell area, each channel was thresholded using Otsu's method and the binary images were added together. Co-localization of the red and green channel was determined to be indicative of compromised cell membranes and excluded from the live cell population. Thus, we calculated live cell area by subtracting the binarized dead cell channel from the live cell channel. Small fragments of cells can remain from this calculation, so we eliminated areas smaller than 50 μm^2 before calculating the live cell area. We validated this approach using the equation, $\% viability = 100\% \times \frac{\#live\,cells}{\#total\,cells}$, for the microgel injectables where single cells are easily identifiable due to low cellular volume fraction and find agreement between the two methods (Figure S15).

5.9. Injection into HA hydrogels and calculations from 3D confocal images

Much like the preparation of samples for AFM, we cast 100 μL of 2% MeHA hydrogels with a 0.7 DTT molar ratio onto 3 cm tissue culture dishes and submerged them in kerosene to prevent evaporation and to mimic the microgel fabrication protocol used here. The samples were crosslinked for 4 h before removing the kerosene and washing with PBS and 0.1% Tween 20. We allowed the samples to swell in PBS overnight before injecting 1 μL mixtures of NSCs and HA microgel or liquid media at a flow rate of 360 μL/h, corresponding to our lowest tested shear rate of 250 s^{-1} (Fig. 5a). The injections were performed by loading the mixtures into our 3D printing syringe and lowering the needle into the hydrogel at 0.1 mm/s to a depth of 0.5 mm from the culture dish bottom. We removed the needle at the same low velocity to minimize damage or displacement of the injected material. Injected NSCs were cultured in this hydrogel for 24 h before introducing

4 mM calcein-AM for 4 h to visualize cells encapsulated in the retained volume, which was measured with confocal microscopy.

Imaging was performed with a 10x objective with a NA of 0.45, where the sampling frequency in the X-Y plane is 1.66 μm and 8.31 μm in the Z-plane. Due to the difference in sampling frequency between the X-Y and Z planes, we interpolate and re-sample data along the Z-axis to create cubic voxels. We perform morphological transformations to fill the gaps between cells, and calculate the total volume occupied by the binary image (Supplementary Information, Figure S16). For data showing protrusion depth (Figure 2), we identify the minimum and maximum z-position manually within the re-sampled 3D stack with detectable fluorescence. The minimum z-position, corresponding to the glass bottom, is designated to be z = 0 μm and the maximum z-position with detectable fluorescence across all RGD concentrations is determined to be 420 μm above the glass bottom. The fluorescence data is masked on a slice-by-slice basis, where data falling at z = 0 μm is given a grayscale value of 1 and data falling at z = 420 μm is given a grayscale value of 255. Data falling on slices between the minimum and maximum z-position is designated an intensity value between 1 and 255 based on its respective z-position. We then take the maximum intensity projection of the 3D stack to identify maximum z-depth of protrusion formation as a function of RGD concentration and time.

5.10. Statistical Analysis

All statistical analyses were performed in GraphPad Prism. Unless otherwise noted, data is presented as mean ± SD. All statistical comparisons were made using a two-tailed t-test. Significance is calculated and reported as * for $p{<}0.05$, ** for $p{<}0.01$, *** for $p{<}0.001$, and **** for $p{<}0.0001$.

Supplementary Material

Refer to Web version on PubMed Central for supplementary material.

Acknowledgements

Data Availability

Data shown and analysis codes generated for this paper is available upon request.

Works Cited

1. Tan H & Marra KG Injectable, biodegradable hydrogels for tissue engineering applications. Materials 3, 1746–1767 (2010).

2. Zhao L, Weir MD & Xu HH An injectable calcium phosphate-alginate hydrogel-umbilical cord mesenchymal stem cell paste for bone tissue engineering. Biomaterials 31, 6502–6510 (2010). [PubMed: 20570346]

3. Adil MM et al. Engineered hydrogels increase the post-transplantation survival of encapsulated hESC-derived midbrain dopaminergic neurons. Biomaterials 136, 1–11 (2017). [PubMed: 28505596]

4. Liu Z et al. The influence of chitosan hydrogel on stem cell engraftment, survival and homing in the ischemic myocardial microenvironment. Biomaterials 33, 3093–3106 (2012). [PubMed: 22265788]

5. Gaffey AC et al. Injectable shear-thinning hydrogels used to deliver endothelial progenitor cells, enhance cell engraftment, and improve ischemic myocardium. The Journal of thoracic and cardiovascular surgery 150, 1268–1277 (2015). [PubMed: 26293548]

6. Liang Y, Walczak P & Bulte JW The survival of engrafted neural stem cells within hyaluronic acid hydrogels. Biomaterials 34, 5521–5529 (2013). [PubMed: 23623429]

7. Tang JD, Roloson EB, Amelung CD & Lampe KJ Rapidly assembling pentapeptides for injectable delivery (RAPID) hydrogels as cytoprotective cell carriers. ACS Biomaterials Science & Engineering 5, 2117–2121 (2019). [PubMed: 33405714]

8. Aguado BA, Mulyasasmita W, Su J, Lampe KJ & Heilshorn SC Improving viability of stem cells during syringe needle flow through the design of hydrogel cell carriers. Tissue Engineering Part A 18, 806–815 (2012). [PubMed: 22011213]

9. Correa S et al. Translational applications of hydrogels. Chemical Reviews 121, 11385–11457 (2021). [PubMed: 33938724]

10. DeForest CA & Anseth KS Cytocompatible click-based hydrogels with dynamically tunable properties through orthogonal photoconjugation and photocleavage reactions. Nature chemistry 3, 925–931 (2011).

11. DeForest CA, Polizzotti BD & Anseth KS Sequential click reactions for synthesizing and patterning three-dimensional cell microenvironments. Nature materials 8, 659–664 (2009). [PubMed: 19543279]

12. Yang J-A, Yeom J, Hwang BW, Hoffman AS & Hahn SK In situ-forming injectable hydrogels for regenerative medicine. Progress in polymer science 39, 1973–1986 (2014).

13. Sharma PK, Taneja S & Singh Y Hydrazone-linkage-based self-healing and injectable xanthan–poly (ethylene glycol) hydrogels for controlled drug release and 3D cell culture. ACS applied materials & interfaces 10, 30936–30945 (2018). [PubMed: 30148349]

14. Bertsch P, Diba M, Mooney DJ & Leeuwenburgh SC Self-healing injectable hydrogels for tissue regeneration. Chemical Reviews 123, 834–873 (2022). [PubMed: 35930422]

15. Moshaverinia A et al. Encapsulated dental-derived mesenchymal stem cells in an injectable and biodegradable scaffold for applications in bone tissue engineering. Journal of Biomedical Materials Research Part A 101, 3285–3294 (2013). [PubMed: 23983201]

16. Grosskopf AK et al. Injectable supramolecular polymer–nanoparticle hydrogels enhance human mesenchymal stem cell delivery. Bioengineering & translational medicine 5, e10147 (2020). [PubMed: 31989036]

17. Cheng J et al. Bone mesenchymal stem cell-derived exosome-loaded injectable hydrogel for minimally invasive treatment of spinal cord injury. Nanomedicine 16, 1567–1579 (2021). [PubMed: 34189939]

18. He S et al. Advances in Injectable Hydrogel Strategies for Heart Failure Treatment. Advanced Healthcare Materials, 2300029 (2023).

19. Jiang X et al. Injectable self-healing cellulose hydrogel based on host-guest interactions and acylhydrazone bonds for sustained cancer therapy. Acta Biomaterialia 141, 102–113 (2022). [PubMed: 34990813]

20. Miller B, Hansrisuk A, Highley CB & Caliari SR Guest–host supramolecular assembly of injectable hydrogel nanofibers for cell encapsulation. ACS Biomaterials Science & Engineering 7, 4164–4174 (2021). [PubMed: 33891397]

21. Chen G & Jiang M Cyclodextrin-based inclusion complexation bridging supramolecular chemistry and macromolecular self-assembly. Chemical Society Reviews 40, 2254–2266 (2011). [PubMed: 21344115]

22. Morley CD et al. Quantitative characterization of 3D bioprinted structural elements under cell generated forces. Nature communications 10, 3029 (2019).

23. Highley CB, Song KH, Daly AC & Burdick JA Jammed microgel inks for 3D printing applications. Advanced Science 6, 1801076 (2019).

24. Ouyang L, Wojciechowski JP, Tang J, Guo Y & Stevens MM Tunable microgel-templated porogel (MTP) bioink for 3D bioprinting applications. Advanced Healthcare Materials 11, 2200027 (2022).

25. Morley CD, Tordoff J, O'Bryan CS, Weiss R & Angelini TE 3D aggregation of cells in packed microgel media. Soft Matter 16, 6572–6581 (2020). [PubMed: 32589183]

26. Muir VG et al. Sticking Together: Injectable Granular Hydrogels with Increased Functionality via Dynamic Covalent Inter-Particle Crosslinking. Small 18, 2201115 (2022).

27. Qazi TH et al. Anisotropic Rod-Shaped Particles Influence Injectable Granular Hydrogel Properties and Cell Invasion (Adv. Mater. 12/2022). Advanced Materials 34, 2270092 (2022).

28. Widener AE, Duraivel S, Angelini TE & Phelps EA Injectable Microporous Annealed Particle Hydrogel Based on Guest–Host-Interlinked Polyethylene Glycol Maleimide Microgels. Advanced NanoBiomed Research 2, 2200030 (2022).

29. Riley L, Schirmer L & Segura T Granular hydrogels: emergent properties of jammed hydrogel microparticles and their applications in tissue repair and regeneration. Current opinion in biotechnology 60, 1–8 (2019). [PubMed: 30481603]

30. Mealy JE et al. Injectable granular hydrogels with multifunctional properties for biomedical applications. Advanced Materials 30, 1705912 (2018).

31. Ananthanarayanan B, Kim Y & Kumar S Elucidating the mechanobiology of malignant brain tumors using a brain matrix-mimetic hyaluronic acid hydrogel platform. Biomaterials 32, 7913–7923 (2011). [PubMed: 21820737]

32. Marklein RA & Burdick JA Spatially controlled hydrogel mechanics to modulate stem cell interactions. Soft Matter 6, 136–143 (2010).

33. Grealish S et al. Human ESC-derived dopamine neurons show similar preclinical efficacy and potency to fetal neurons when grafted in a rat model of Parkinson's disease. Cell stem cell 15, 653–665 (2014). [PubMed: 25517469]

34. Kriks S et al. Dopamine neurons derived from human ES cells efficiently engraft in animal models of Parkinson's disease. Nature 480, 547–551 (2011). [PubMed: 22056989]

35. Regmi S, Fu A & Luo KQ High shear stresses under exercise condition destroy circulating tumor cells in a microfluidic system. Scientific reports 7, 39975 (2017). [PubMed: 28054593]

36. Leverett L, Hellums J, Alfrey CP & Lynch EC Red blood cell damage by shear stress. Biophysical journal 12, 257–273 (1972). [PubMed: 5016112]

37. Food U & Administration D Guidance for FDA reviewers and sponsors: Content and review of chemistry, manufacturing, and control (CMC) information for human somatic cell therapy investigational new drug applications (INDs). Center for Biologics Evaluation and Research (2008).

38. Bhattacharjee T et al. Polyelectrolyte scaling laws for microgel yielding near jamming. Soft matter 14, 1559–1570 (2018). [PubMed: 29450413]

39. Vernon B, Kim SW & Bae YH Insulin release from islets of Langerhans entrapped in a poly (N-isopropylacrylamide-co-acrylic acid) polymer gel. Journal of Biomaterials Science, Polymer Edition 10, 183–198 (1999). [PubMed: 10091930]

40. Lee MS, Lill M & Makkar RR Stem cell transplantation in myocardial infarction. Reviews in cardiovascular medicine 5, 82–98 (2004). [PubMed: 15184842]

41. Hoeeg C, Dolatshahi-Pirouz A & Follin B Injectable hydrogels for improving cardiac cell therapy —in vivo evidence and translational challenges. Gels 7, 7 (2021). [PubMed: 33499287]

42. Rehfeldt F, Engler AJ, Eckhardt A, Ahmed F & Discher DE Cell responses to the mechanochemical microenvironment—implications for regenerative medicine and drug delivery. Advanced drug delivery reviews 59, 1329–1339 (2007). [PubMed: 17900747]

43. Rosales AM, Vega SL, DelRio FW, Burdick JA & Anseth KS Hydrogels with reversible mechanics to probe dynamic cell microenvironments. Angewandte Chemie International Edition 56, 12132–12136 (2017). [PubMed: 28799225]

44. Barattin R & Voyer N Chemical modifications of atomic force microscopy tips. Atomic Force Microscopy in Biomedical Research: Methods and Protocols, 457–483 (2011).
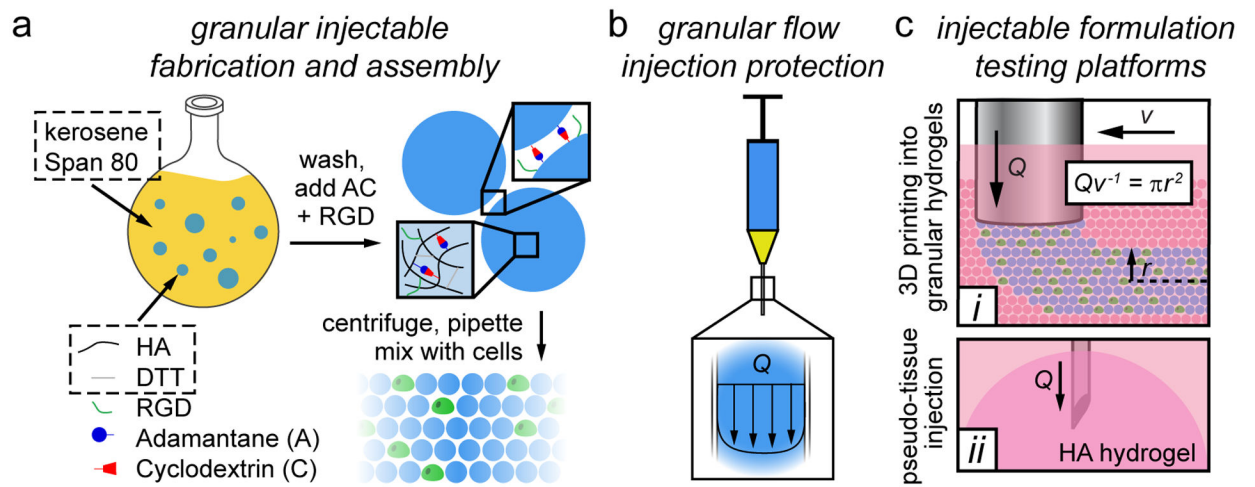
45. Kubrova E et al. Hypothermia and nutrient deprivation alter viability of human adipose-derived mesenchymal stem cells. Gene 722, 144058 (2020). [PubMed: 31494240]

Figure 1. Microgel-based injectable assembly and testing platform.
(a) Inverse emulsion polymerization process of MeHA and DTT. Residual methacrylate groups are used for functionalization with AC and RGD-based cell adhesion peptides. Cells are encapsulated between these microgel particles to (b) facilitate injection protection and provide a stable 3D engraftment niche post-injection. (c) 3D printing platform used to facilitate the study of injection protection and retention.
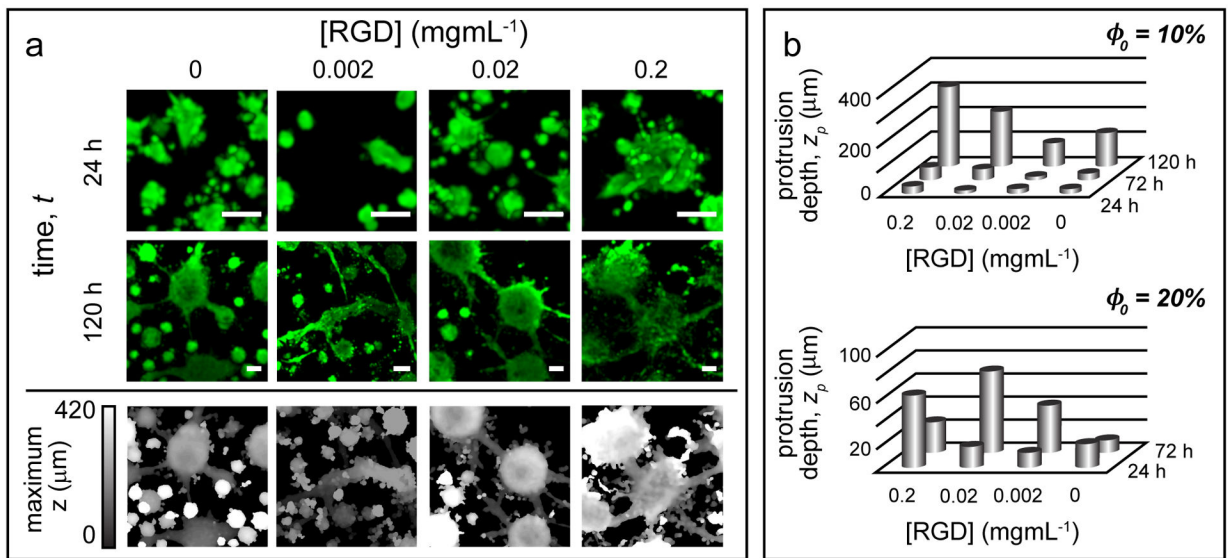
Figure 2. Quantifying 3D NSC attachment.
(a) Representative images of the dominant morphological phenotype for each RGD concentration and $\phi_0 = 10\%$ – (top) maximum intensity projection of raw fluorescent data – (bottom) grayscale height map used to calculate protrusion depth. Scale bars = 50 μm. (b) Quantification of maximum protrusion depth as a function of seeding density, ϕ_0, and time, t. Bars represent the mean maximum protrusion depth (n = 3–5 measurements).
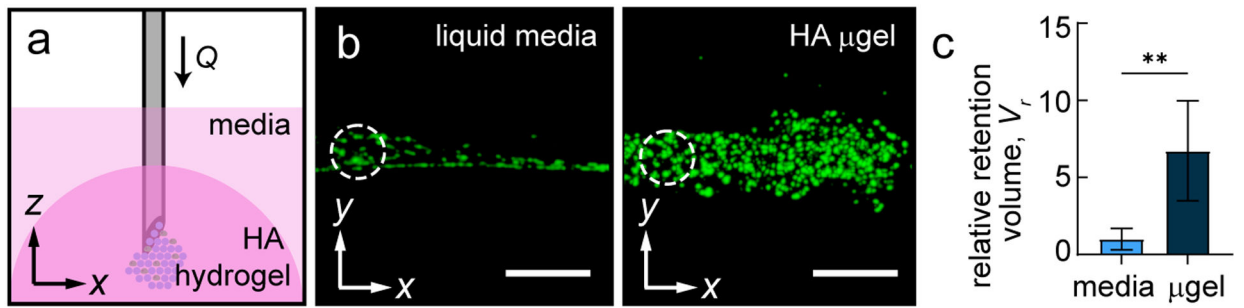
**Figure 3. Retaining injected cellular cargo.**
(a) Injection into hydrogels to measure volume retention capacity of granular materials. (b) Representative images of NSC-laden liquid (left) and NSC-laden microgel (right) injectable. Images shown are maximum intensity projections of confocal z-stacks. White dotted circle represents the 30G needle diameter. Scale bar = 250 μm. (c) Quantification of relative retention volume, V_r (n=3 samples, data reported as mean ± standard deviation, $p<0.01$).
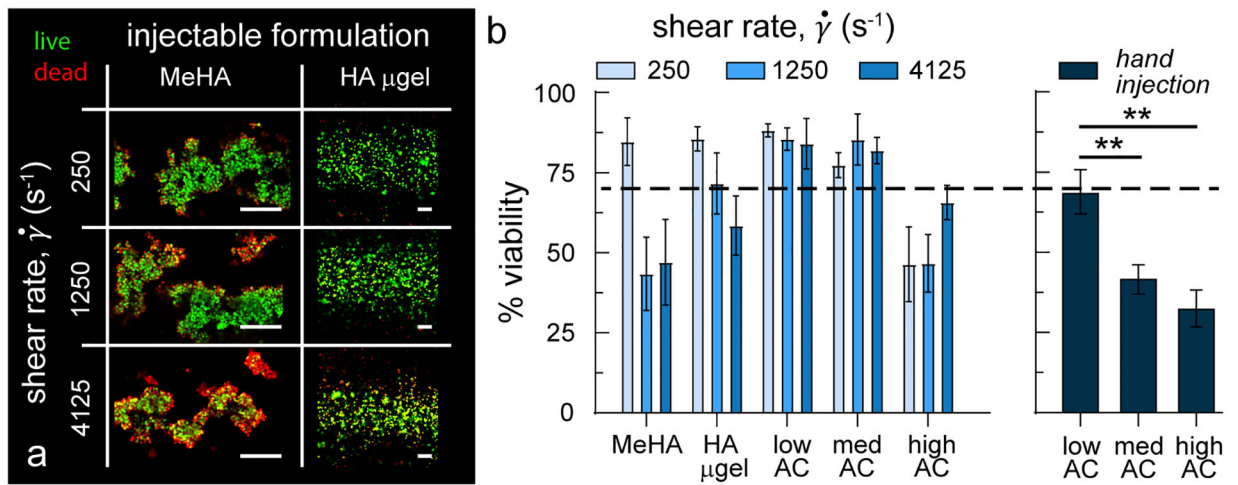
Figure 4. 3D printing injectable formulations into bare HA microgels.
(a) Live (green) and dead (red) cells after 24 h in culture post-injection into our 3D printing sacrificial microgel material. Scale bar = 100 μm. Quantification of viability for cells injected (b) at controlled shear rates on the 3D printer and hand injected. Dashed line corresponds to the 70% viability target. Data reported as mean ± standard deviation (n = 3 samples). Annotations of statistical significance are omitted (left) for clarity.
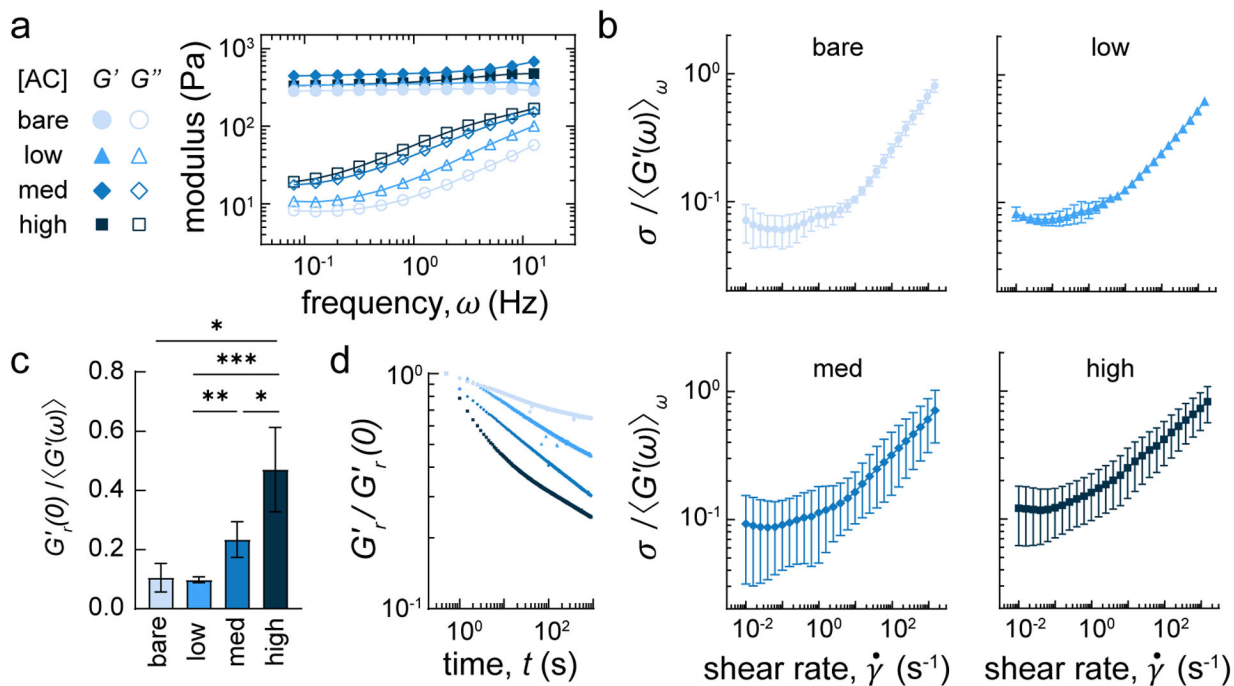
Figure 5. Rheological characterization of HA-AC microgels.
(a) Oscillatory rheology shows $G' > G''$ and frequency independence of G' for all AC concentrations. (b) Unidirectional rheology is normalized by $\langle G'(\omega)\rangle_\omega$, from the oscillatory sweep to determine if they behave like HB yield stress fluids. Data reported as mean and error bars represent the minimum and maximum σ (n=3 samples) for a given $\dot{\gamma}$. (c) Peak relaxation modulus normalized by $\langle G'(\omega)\rangle_\omega$ to quantify the maximum stress upon instantaneous deformation. (d) Full stress relaxation data normalized by $G'_r(0)$.

indentation analysis
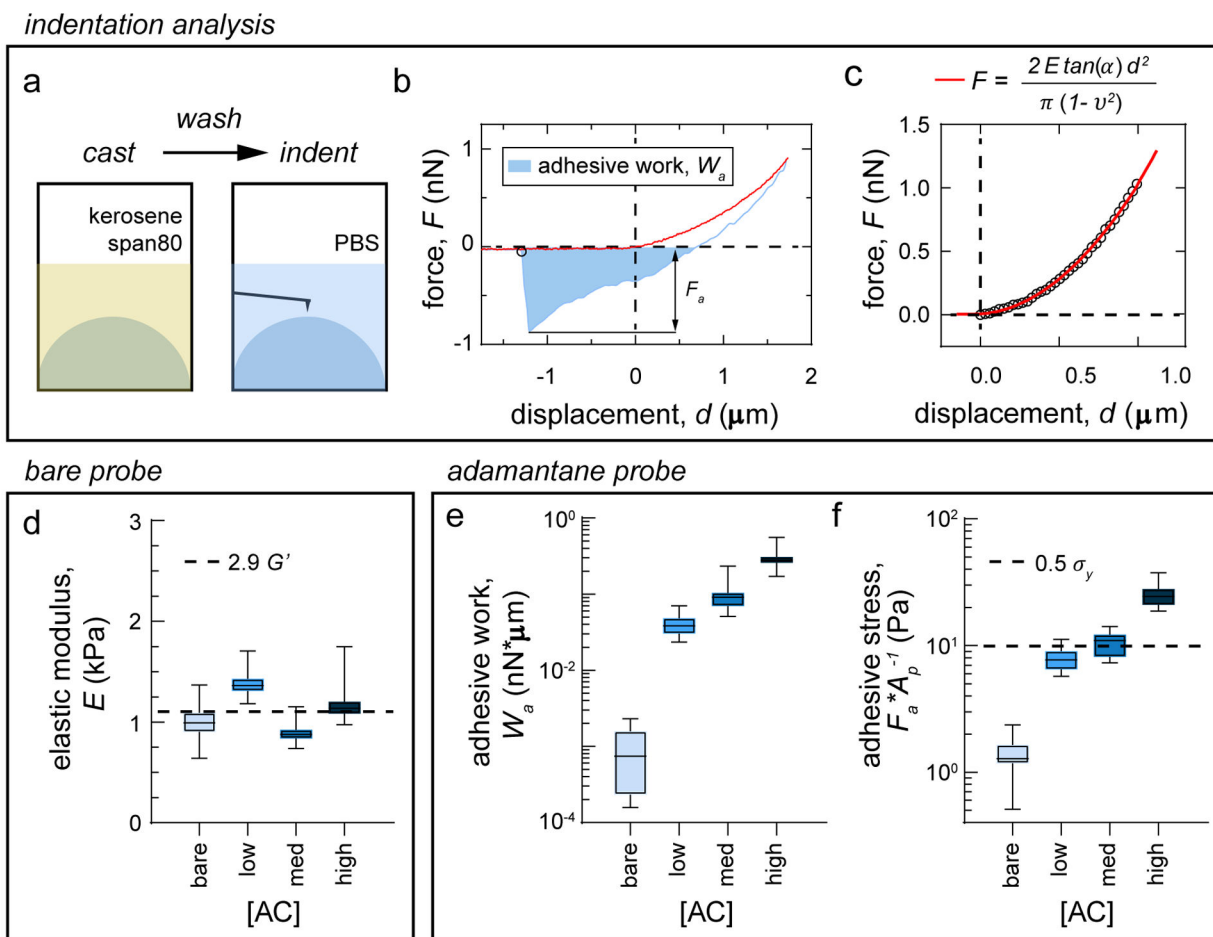
Figure 6. AFM on HA-AC hydrogels.
(a) Sample preparation for AFM measurements. (b) Representative indentation and retraction curve including calculated metrics for quantifying adhesion. (c) Representative indentation curve fitting using the approximation of Hertzian conical contact. (d) Young's modulus values from curves acquired on samples with a bare probe. (e) Adhesive work and (f) adhesive stress calculation for AC samples indented with an adamantane functionalized probe. Box plots display the IQR and whiskers represent the 1st and 99th percentiles (n=100 indentations with the bare probe and 36 indentations with the adamantane-functionalized probe). Annotations of statistical significance are omitted for clarity. Adhesive stress measurements between low and med AC concentrations significantly differ from one another by t-test ($p<0.001$). All other adhesive work and stress measurement comparisons significantly differ from one another by t-test ($p<0.0001$).
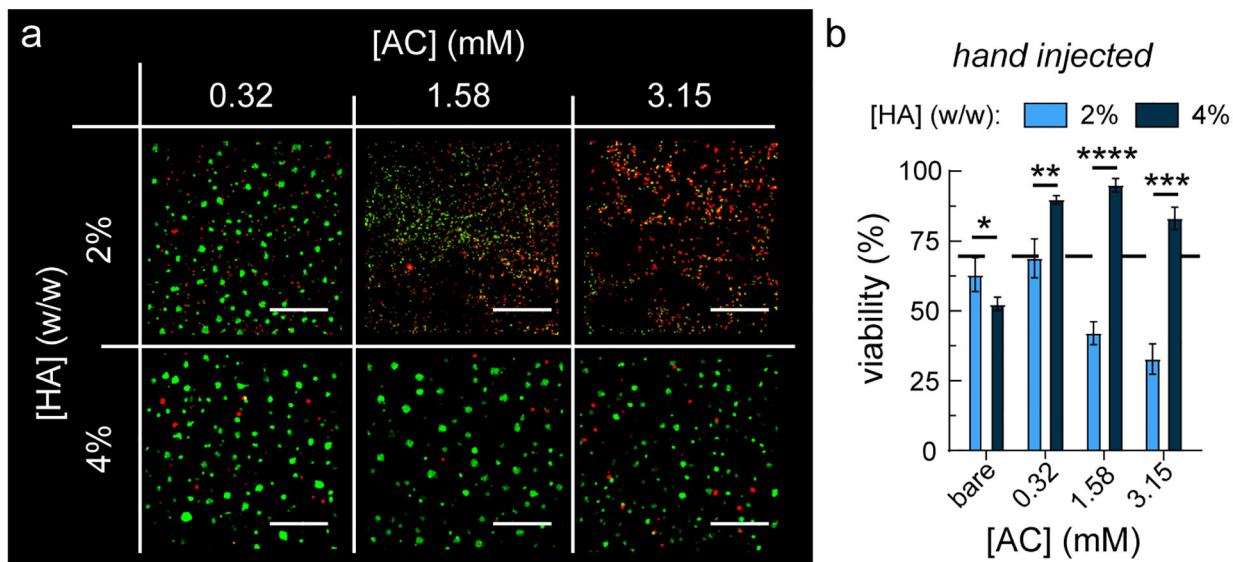
Figure 7. Injection with stiffer microgels increases NSC viability.
(a) Viability of NSCs after injection with 2 – 4% (w/w) HA microgels functionalized with 0.32 – 3.15 mM AC. Scale bar = 250 μm. (b) Quantification of viability. Data reported as mean ± standard deviation (n=3 samples).

Table 1.

Fitted values for rheological characterization (Figure 5b,d). Fitted parameters σ_y and $\dot{\gamma}_c$ (Methods) are not calculable for med and high AC concentrations since they do not behave as HB yield stress fluids.

[AC]	σ_y/G'	$\dot{\gamma}_c$ (1/s)	p	β
bare	0.06	6.60	0.49	0.07
low	0.07	10.53	0.43	0.12
med	N/A	N/A	0.36	0.15
high	N/A	N/A	0.29	0.27

Table 2.

AC solution molarity corresponding to each molar ratio.

	AC:HA molar ratio		
	0.01	**0.05**	**0.11**
Final AC concentration (mM)	0.32	1.58	3.15